Qualitative and Quantitative MR Imaging of the Cartilaginous Endplate: A Review

Zhao Wei, PhD,[1,2] Jiyo S. Athertya, PhD,[2] Christine B. Chung, MD,[2,3] Graeme M. Bydder, MB, ChB,[2] Eric Y. Chang, MD,[2,3] Jiang Du, PhD,[2,3,4] Yang Wenhui, ME,[1,5] and Yajun Ma, PhD[2*]

The cartilaginous endplate (CEP) plays a pivotal role in facilitating the supply of nutrients and, transport of metabolic waste, as well as providing mechanical support for the intervertebral disc (IVD). Recent technological advances have led to a surge in MR imaging studies focused on the CEP. This article describes the anatomy and functions of the CEP as well as MRI techniques for both qualitative and quantitative assessment of the CEP. Effective CEP MR imaging sequences require two key features: high spatial resolution and relatively short echo time. High spatial resolution spoiled gradient echo (SPGR) and ultrashort echo time (UTE) sequences, fulfilling these requirements, are the basis for most of the sequences employed in CEP imaging. This article reviews existing sequences for qualitative CEP imaging, such as the fat-suppressed SPGR and UTE, dual-echo subtraction UTE, inversion recovery prepared and fat-suppressed UTE, and dual inversion recovery prepared UTE sequences. These sequences are employed together with other techniques for quantitative CEP imaging, including measurements of T_2*, T_2, T_1, $T_{1\rho}$, magnetization transfer, perfusion, and diffusion tensor parameters.
Evidence Level: 1
Technical Efficacy: Stage 2

J. MAGN. RESON. IMAGING 2024.

Low back pain affects up to 26% of adults in the United States, and may severely affect their life and work.[1,2] One of the primary causes of low back pain is intervertebral disc (IVD) degeneration.[3–5] The IVD is a crucial component of the spinal column. It carries a variety of mechanical loads arising from bodily weight and muscle activity including torsion and flexion. The IVD is composed of a circular annulus fibrosus (AF) and a central nucleus pulposus (NP), which are sandwiched between superior and inferior cartilaginous endplates (CEPs).[6] The CEP plays a pivotal role in the degeneration process of IVD. Serving as the primary conduit for nutrients entering and waste exiting the IVD, the endplate (include the bony endplate and CEP) also acts as a mechanical barrier to prevent the NP bulging into the adjacent vertebral body.[7–9] Loss of large proteoglycan molecules and calcification of the CEP tissue reduce the permeability of nutrient into the NP and AF, leading to the degeneration of IVD.[3,7,10,11] Moreover, CEP fractures disrupt hydration and force distribution from the NP, allowing fluid to flow from the NP to the adjacent vertebral body under loading. This results in NP decompression and further degeneration.[12,13] Additionally, CEP damage decreases its ability to sieve cells and macromolecules, facilitating inflammatory crosstalk between the IVD and bone marrow in Modic changes, thereby accelerating degeneration associated with Modic changes.[14] Accurate diagnosis of CEP damages is essential for the pathological study of IVD degeneration and Modic Changes. However, the CEP has received relatively little attention in MRI due to its thinness, and the limitations of many MR techniques in detecting signal from it. This is unlike the detailed exploration of the anatomy and pathophysiology of the NP and AF which have received a lot of attention with MRI. In recent years, technological advances, particularly including the development of ultrashort echo time (UTE) sequences, have led to a large increase in MR imaging studies of the CEP.

View this article online at wileyonlinelibrary.com. DOI: 10.1002/jmri.29562

Received Jun 5, 2024, Accepted for publication Jul 26, 2024.

*Address reprint requests to: Y.M., 9452 Medical Center Dr., San Diego, CA 92037, USA. E-mail: yam013@ucsd.edu

From the [1]Institute of Electrical Engineering, Chinese Academy of Sciences, Beijing, China; [2]Department of Radiology, University of California San Diego, San Diego, California, USA; [3]Radiology Service, Veterans Affairs San Diego Healthcare System, San Diego, California, USA; [4]Department of Bioengineering, University of California San Diego, San Diego, California, USA; and [5]University of Chinese Academy of Sciences, Beijing, China

This review aims to describe these techniques and their use in the study of the CEP.

Anatomy and Physiology of the Cartilaginous Endplate

Figure 1 shows the structure of a normal IVD along with a small section of the superior and inferior vertebral bodies. The superior and inferior CEPs are thin layers of hyaline-like cartilage, ranging in thickness from 0.1 mm to 1.6 mm,[3] which cover the cranial and caudal ends of the inner AF and NP. The CEPs separate the IVD from the vertebral bony endplates. CEP thickness varies with tissue region (thicker in the peripheral and thinner in the center) and age (decreasing with increased age).[15–17] The CEP is mainly composed of water (55%), collagen (25%), and proteoglycans (8%).[6]

The CEP functions as a pathway for the diffusion of nutrients from the peripheral vasculature in the adjacent vertebral body and for waste out of the IVD into the venous system of the IVD. These roles are crucial as the IVD is the largest avascular structure in the human body.[10] Oxygen and glucose are transported into the IVD through the CEP.[18,19] Degradation and calcification of the CEP affect the health of the IVD by influencing vertebral perfusion and nutrient diffusion.[3,7] The CEP permeability is essential for maintaining fluid pressurization within the NP, which helps to uniformly distribute the stress across the IVD.[8] However, CEP permeability decreases with aging due to the occlusion of vascular canals caused by ectopic calcification, a reduction in glycosaminoglycan content, and an increase in calcium-binding collagen type X within the CEP.[7,20–22]

Moreover, the CEP plays an important role in mechanically constraining the disc and preventing the NP from bulging into the adjacent vertebral body. The CEPs also provide cranial and caudal anchorages for NP and inner AF fibers.[23,24] Finite element model analysis has also illustrated that the structure and mechanics of the CEP may play a key role in disc mechanics.[25] Morphological abnormalities in the CEP, such as fractures, avulsion, and Schmorl's nodes, are frequently observed and correlate with progression of IVD degeneration.[26,27] Thus, accurate diagnosis of CEP abnormalities is crucial for understanding the mechanisms of IVD degeneration and its associated low back pain.

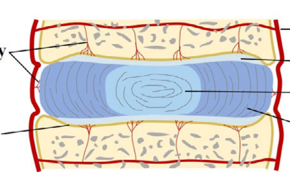

FIGURE 1: A diagram depicting the sagittal cross-section of an intervertebral disc, which is positioned between the superior and inferior vertebral bodies.

MRI of the Cartilaginous Endplate

MRI is routinely used to assess IVD degeneration,[28,29] and offers insights into its anatomy, composition, and degeneration by using techniques which take advantage of MRI's high soft tissue contrast compared with other imaging modalities, such as X-Ray and CT. The pivotal role of MRI in the diagnosis and staging of IVD degeneration includes recent advances in IVD regeneration.

MRI studies on IVD degeneration have predominantly focused on imaging the NP and AF tissues.[30–37] CEP imaging using MRI is challenging due to its thinness[3,13] and short T_2/T_2^* relaxation times.[38–41] The reported CEP T_2 and T_2^* value ranges are 17.79 msec–66.34 msec[39,41] and 2.9 msec–43 msec,[38,40,42,43] respectively, considerably short in comparison with the commonly used echo times (TEs) of conventional clinical T_1-weighted (T_1w) and T_2-weighted (T_2w) fast spin echo (FSE) MRI sequences. Consequently, the CEP appears hypointense on conventional T_1w- and T_2w-FSE images, rendering it indistinguishable from bony endplates.[28] Fortunately, several sequences, such as spoiled gradient echo (SPGR)-based[15–17,44–46] and ultrashort echo time (UTE)-based[38,40,42,43,47–55] sequences can address this problem. Applications of these pulse sequences in CEP imaging are described below.

Qualitative MRI of the Cartilaginous Endplate

SPGR SEQUENCES. SPGR sequences meet the two essential requirements for CEP imaging: high spatial resolution and relatively short TE.[56] SPGR, commonly characterized by a low flip angle, is a gradient echo pulse sequence in which the echo signal is spoiled using a gradient. This enables the sequence to achieve a relatively short TE and rapid longitudinal relaxation recovery. Studies have reported a TE of 3.7 msec and repetition time (TR) of 9 msec for CEP imaging with SPGR sequence,[15–17] resulting in images being T_1-weighted. The SPGR sequence is readily available on clinical scanners and allows shorter scan times for the same field of view than UTE pulse sequences.[17]

Beattie et al employed the 3D SPGR sequence to create the CEP contrast and subsequently measure CEP spatial parameters.[16] The CEP contrast enhancement capability of the SPGR underscores its potential for quantifying CEP dimensions and evaluating structural changes in the CEP associated with disc degeneration.

SPGR sequences with fat suppression (FS) further improve the contrast between the CEP and adjacent tissues, such as the bone marrow fat (BMF) within vertebra and NP.[15,17,45,46] In 2002, Kakitsubata et al applied a 3D FS-SPGR sequence on 48 CEP specimens, showcasing its efficacy in enhancing CEP visualization.[46] In 2013 and 2016, Moon and Delucca et al applied 3D FS-SPGR sequences with optimized flip angle and TR to enhance CEP-NP and

CEP-BMF contrasts for visualizing CEP structure and measuring CEP thickness distribution.[15,17] Most recently, Athertya et al optimized a T_1w 3D FS-SPGR sequence for high contrast CEP imaging in vivo (Fig. 2a).[45] A product SPECtral Inversion At Lipid (SPECIAL) technique was utilized for fat suppression. The 3D FS-SPGR sequence is adept at demonstrating both normal CEP morphology (Fig. 2d) and CEP abnormalities (Fig. 2g), and is well suited to clinical applications.

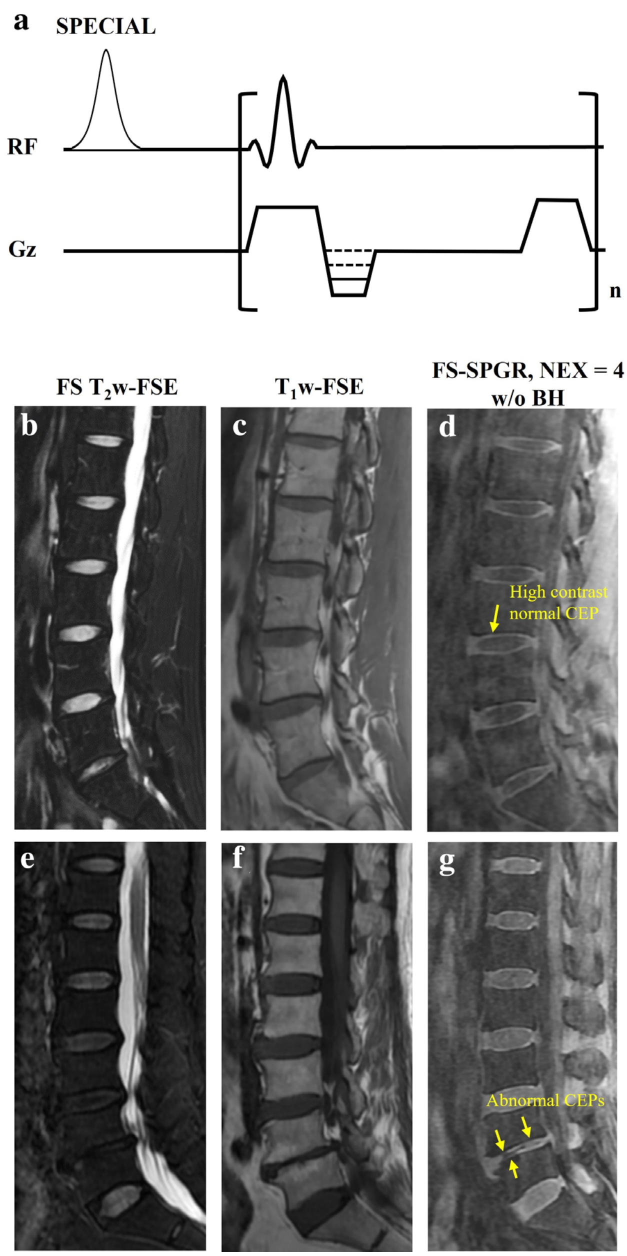

FIGURE 2: Cartilaginous endplate (CEP) imaging using a 3D fat-suppressed spoiled gradient echo (FS-SPGR) sequence. The fat suppression was achieved with SPECtral Inversion At Lipid (SPECIAL) (a). Clinical T_2 weighted fast spin echo (T_2w-FSE) (b, e) and T_1 weighted FSE (T_1w-FSE) (c, f) images as well as 3D FS-SPGR images (d, g) were obtained from a 32-year-old healthy male (second row) and a 67-year-old female with lower back pain (third row). The CEP structures in normal and abnormal CEP regions are indicated by yellow arrows in panels (d) and (g), respectively. Reproduced with permission from Athertya et al.[45]

UTE SEQUENCES. UTE-type sequences are widely used in musculoskeletal system imaging owing to their capacity to detect fast decaying signals from short and ultrashort T_2 tissues.[57] As early as 2004, Gatehouse et al confirmed the feasibility of visualizing CEP tissue using a 2D UTE (Fig. 3a), 2D FS-UTE, and 2D FS-UTE with long T_2 tissues suppression.[53] Figure 3d shows a 3D UTE sequence with a Cones sampling trajectory.[52,58] This sequence initiates data acquisitions immediately after a slab selective half pulse excitation, enabling the TE to be minimized. The minimum TEs of 2D and 3D UTE sequences can be as short as 8 μs.[59,60] CEP structures on UTE images are high signal (Fig. 3b,e), compared with the low signal on clinical T_1w-SE (Fig. 3c) and T_2w-FSE images (Fig. 3f).

In recent years, with advances in UTE techniques, an increasing number of UTE-based methods have been used for CEP imaging. In 2012, Bae et al utilized the 2D UTE subtraction technique to visualize calcified and uncalcified CEP morphology.[49] In 2013, Law et al reported on the feasibility of the 3D UTE technique for assessing CEP defects, and found a significant association between the presence of CEP defects and IVD degeneration.[50] In 2018, Berg-Johansen et al measured the CEP thickness with 3D FS-UTE sequence, and revealed that the CEP thickness was greater at the periphery and smaller at the central portion and the heterogeneity in CEP thickness might serve as an indicator of IVD degeneration.[48]

In 2023, Ji et al employed a 3D fast dual-echo UTE technique to obtain subtracted images of CEPs, which displayed the CEP structure well with high contrast between the CEP and the bony vertebral endplate.[47] This technique may serve as an effective tool for evaluating CEP damage. Lombardi et al introduced a 3D adiabatic inversion-recovery-prepared fat-saturated UTE (IR-FS-UTE) sequence (Fig. 4a) designed to highlight CEP contrasts relative to the NP and BMF.[52] This sequence employed an IR pulse to effectively suppress signals from long T_1 tissues (eg, NP), followed by a fat saturation module to suppress fat signals. The IR-FS-UTE sequence produced high contrast CEP images both in vivo (Fig. 4b–e) and ex vivo (Fig. 5). Most recently, Athertya et al compared the CEP image contrast produced by various UTE-based techniques, including dual adiabatic inversion recovery prepared UTE (DIR-UTE) (Fig. 6a), IR-FS-UTE (Fig. 4a), and T_1w-FS-UTE.[51] All these UTE techniques could image CEP with high contrast. Among these methods, DIR-UTE generated the highest CEP contrast, followed by IR-FS-UTE and T_1w-FS-UTE. The DIR-UTE method used two narrow-band adiabatic full passage pulses to efficiently suppress long T_2 water and fat simultaneously and selectively imaged short T_2 CEP. The study

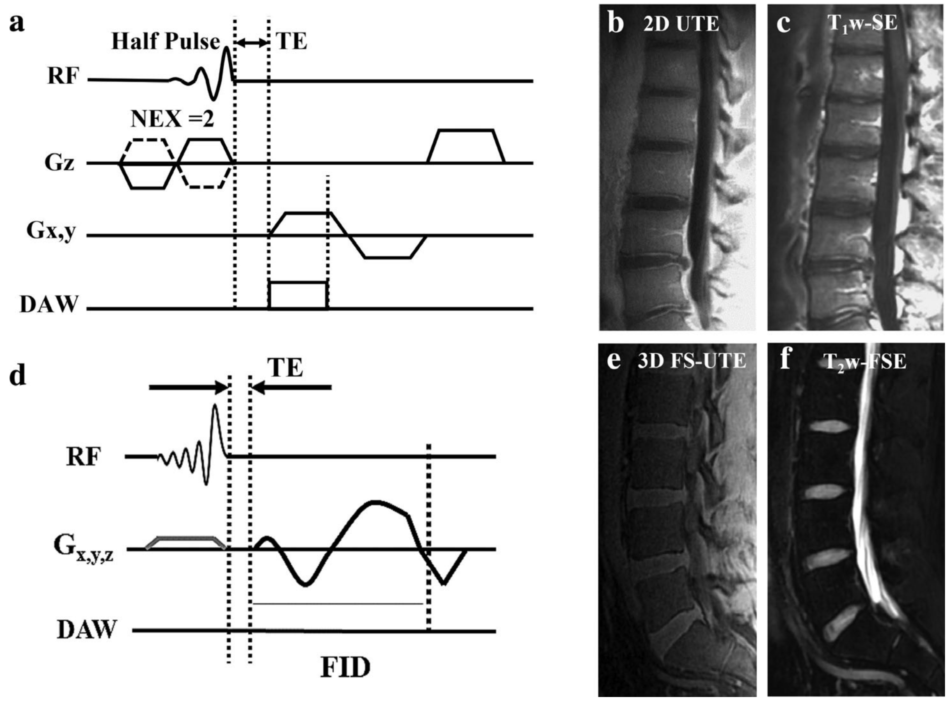

FIGURE 3: 2D and 3D ultrashort echo time (UTE) imaging of the cartilaginous endplate (CEP). Diagrams of 2D and 3D UTE sequences are shown in (**a**) and (**d**), respectively, accompanied by lumbar spine images acquired with the 2D UTE (**b**), fat suppressed 3D UTE (3D FS-UTE) (**e**), T_1 weighted spin echo (T_1w-SE) (**c**), as well as T_2 weighted fast spin echo (T_2w-FSE) (**f**) sequences. CEP structures are visible on UTE images but are invisible on clinical T_1w-SE and T_2w-FSE images. (**b**, **c**) Reproduced with permission from Gatehouse et al.[53] (**d**) reproduced with permission from Lombardi et al.[52]

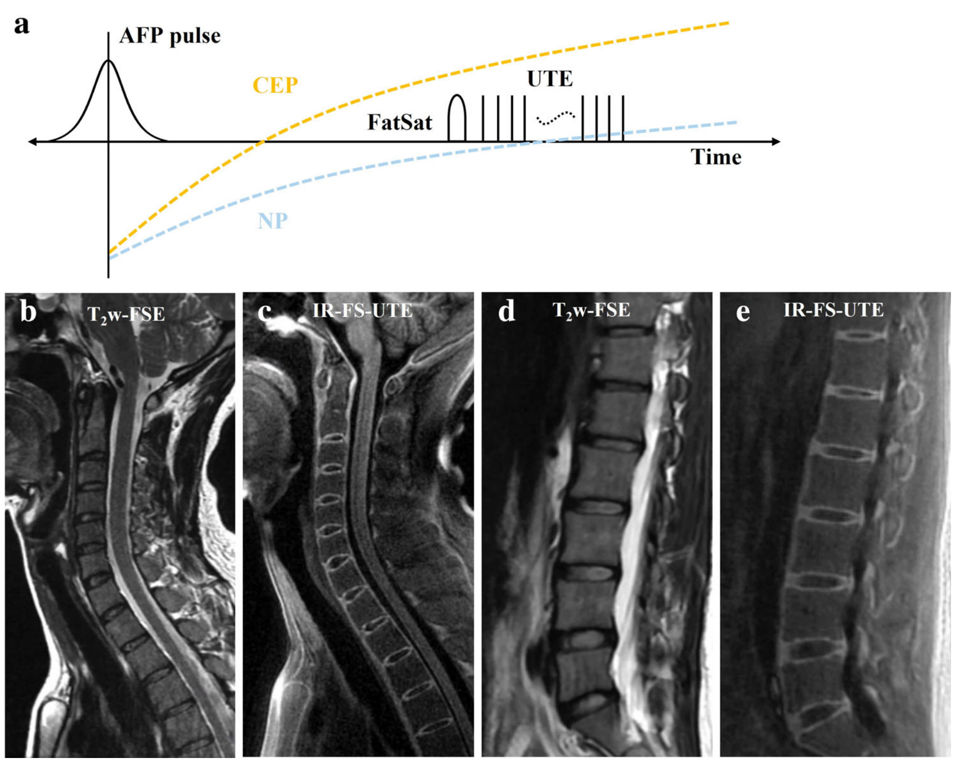

FIGURE 4: Cartilaginous endplate (CEP) imaging with an inversion recovery fat suppression ultrashort echo time (IR-FS-UTE) sequence. (**a**) shows the CEP contrast mechanism for the IR-FS-UTE sequence. The signals from the nucleus pulposus (NP) are suppressed by the adiabatic full passage (AFP) IR pulse to improve CEP contrast with the NP, and the fat signals are suppressed by the fat saturation (FatSat) pulse to improve CEP contrast with bone marrow fat. Multiple UTE spokes are sampled after each IR and FatSat preparation. Cervical and lumbar spine images of a 30-year-old female volunteer are shown in (**b–e**). The clinical T_2 weighted fast spin echo (T_2w-FSE) images (**b**, **d**) cannot capture CEP signals, while the IR-FS-UTE highlights CEP regions (**c**, **e**).

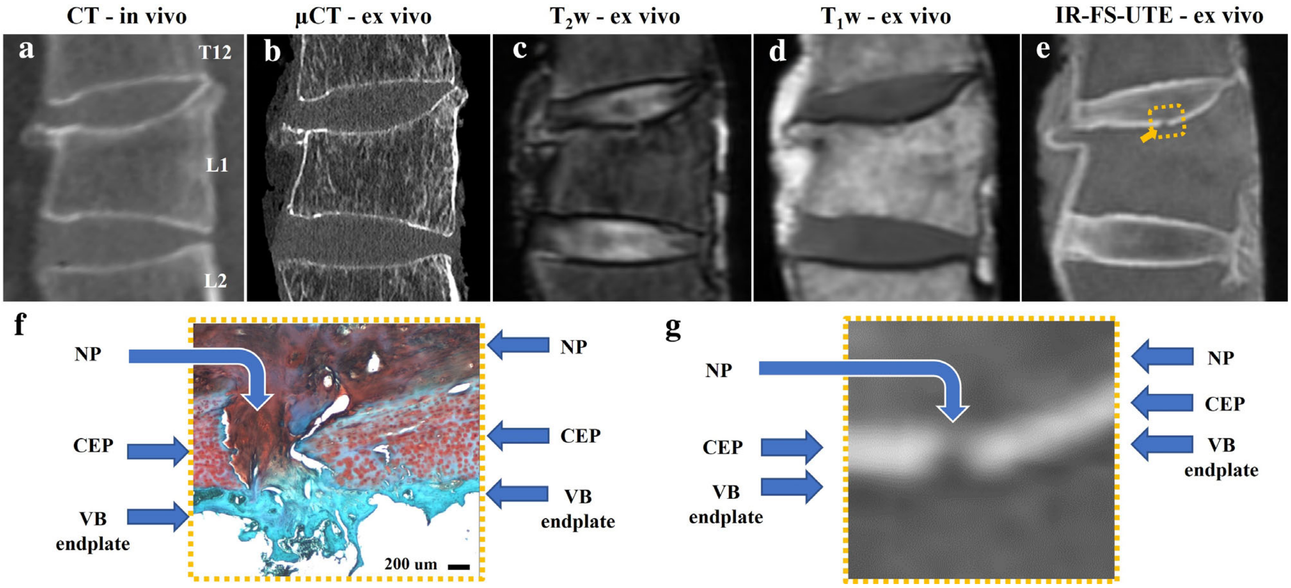

FIGURE 5: Cartilaginous endplate (CEP) imaging of a spine sample. Images of T12-L2 from in vivo CT scan (**a**) obtained prior to the patient's (68-year-old female donor) death and postmortem ex vivo μCT scan (**b**), clinical T_2 weighted- and T_1 weighted-fast spin echo (T_2w-FSE and T_1w-FSE) (**c**, **d**), as well as inversion recovery fat suppression ultrashort echo time (IR-FS-UTE) sequences (**e**). As shown on the IR-FS-UTE image (**e**) by a yellow arrow, there is a CEP fracture in the superior endplate of L1 with herniation of the nucleus pulposus (NP) through the focal defect which is confirmed with histology (**f**) and (**g**) is the magnified fracture region (yellow box) on the IR-FS-UTE image (**e**). VB endplate = vertebral bony endplate. Reproduced with permission from Lombardi et al.[52]

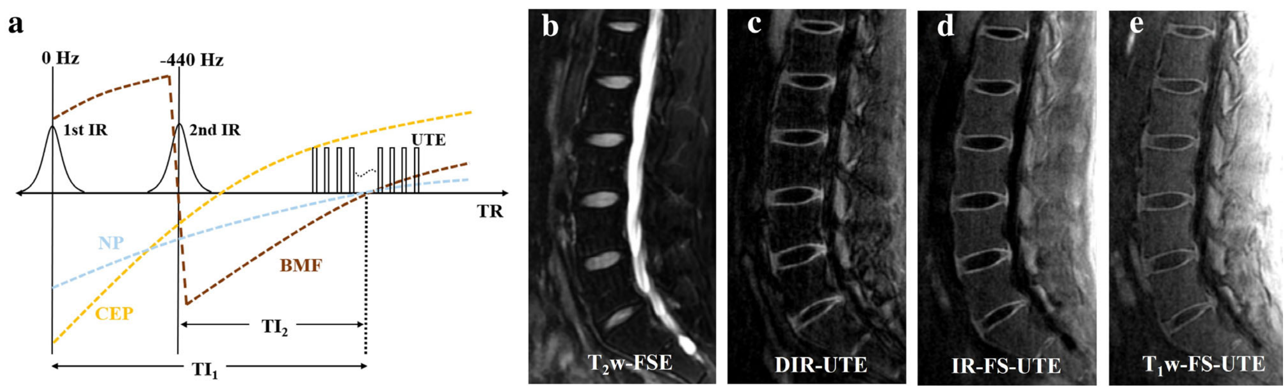

FIGURE 6: Cartilaginous endplate (CEP) imaging using a dual inversion recovery-prepared ultrashort echo time (DIR-UTE) sequence. The CEP contrast mechanism for the DIR-UTE sequence is shown in (**a**). This sequence utilizes two adiabatic full passage pulses to invert long T_2 water (eg, nucleus pulposus [NP]) and bone marrow fat (BMF) with center frequencies of 0 and −440 Hz, respectively, followed by multiple UTE spoke acquisition. Lumbar spine images of a 38-year-old asymptomatic male volunteer acquired with clinical T_2 weighted fast spin echo (T_2w-FSE) (**b**), DIR-UTE (**c**), inversion recovery fat suppression ultrashort echo time (IR-FS-UTE) (**d**), and T_1 weighted FS-UTE (T_1w-FS-UTE) (**e**) sequences. The DIR-UTE sequence provides the best CEP contrast in comparison to other UTE-based techniques.

also demonstrated that the DIR-UTE method could detect morphological CEP abnormalities, such as CEP discontinuity and erosive node. The major weakness of DIR-UTE and IR-FS-UTE techniques is their relatively long scan time. In comparison, the T_1w-FS-UTE technique shows promise for clinical use due to its great scan efficiency and reasonable CEP contrast.

Studies have shown that CEP thickness was related to age and region but not to IVD levels.[15–17,48] The thickness is smallest at the center and greatest at periphery.[15–17] Averaged CEP thickness reported in References 15, 16, 17, and 48 are 0.58 mm, 0.5 mm, 0.77 mm, and 0.74 mm, respectively, as shown in Table 1. However, the mean CEP thickness measured with histological methods are 0.62 mm and 0.47 mm in References 3 and 13, respectively. Although the MRI-derived CEP thickness measurements are slightly overestimated compared to histological measurements, their reliabilities were confirmed by significant correlations with corresponding histological measurements in same location within the IVD.[17,48]

Table 1 summarizes qualitative CEP imaging studies. The SPGR sequence captures the CEP signal with a

TABLE 1. Qualitative MRI Techniques for Cartilaginous Endplate Imaging

Techniques	Applications	Scanner and Key Sequence Parameters	Advantages and Limitations	Main Findings
3D SPGR[16]	Measurement of CEP structure.	7 T (Siemens); TR/TE = 9/3.7 msec; resolution = 0.2 × 0.2 × 0.2 mm^3; scan time = 3 minutes	Advantages: • Time efficient and clinically available. Limitations: • CEP-NP and CEP-BMF contrasts were limited.	• CEP thickness was greatest at anterior/posterior margins, and smallest in the center. • CEP thickness was not associated with disc level. • The mean CEP thickness was 0.5 mm.
3D FS-SPGR[15,17,45,46]	• High contrast CEP imaging. • Evaluate relationships between CEP structural measurements and age, IVD degeneration, spinal level, and disc morphology.	Reference 15: 7 T (Siemens); TR/TE = 9/3.7 msec; resolution = 0.2 × 0.2 × 0.2 mm^3; scan time = 3 minutes (ex vivo) Reference 45: 3 T (GE MR750); TR/TE = 5.1/2 msec; in-plane resolution = 0.9 × 1.3 mm^2; scan time = 24 seconds for NEX = 1. Reference 17: 7 T (Siemens); TR/TE = 9/3.7 msec; resolution = 0.2 × 0.2 × 0.2 mm^3; scan time = 6 minutes (ex vivo) In vivo: 3 T (Siemens, Tim Trio); TR/TE = 9/3.7 msec; in-plane resolution = 0.4 × 0.4 mm^3. Reference 46: 1.5 T (GE Signa); TR/TE = 38/8 msec; in-plane resolution = 0.78 × 1.3 mm^2.	Advantages: • Time efficient and clinically available. • FS module provides high CEP-BMF contrast. • Free-breathing with high CNR.[45] Limitations: • Need high NEX to maintain sufficient SNR. • Fat suppression efficiency may be limited.	• CEP thickness was greatest at anterior/posterior margins, and smallest in the center.[15,17] • Mean CEP thickness were 0.58 mm[15] and 0.77 mm.[48] • 3D FS-SPGR sequence detected various morphologic abnormalities of the CEP.[45]

TABLE 1. Continued

Techniques	Applications	Scanner and Key Sequence Parameters	Advantages and Limitations	Main Findings
2D UTE 2D FS-UTE 2D FS-LS-UTE[a,53]	Improve the contrast of CEP.	1.5 T (Siemens, Sonata); TR = 500 msec; TE = 0.08, 5.95, 11.08, 17.70 msec.[3]	Advantages: • Short TE and detect the CEP signal with a high SNR. Limitations: • Not widely available for clinical.	These UTE techniques can detect CEP signals with high contrast relative to adjacent tissues.
2D UTE dual-echo subtraction[49]	Improve the contrast of CEP.	3 T (GE Signa HDx); TR = 300 msec; TE_1 = 0.008 msec; TE_2 = 6.6 msec	Advantages: • Increased CEP-NP contrast. Limitations: • Limited CEP-BMF contrast. • Suffer susceptibility-induced signal variations.	• 2D UTE images enable visualization of the uncalcified and calcified CEP. • 2D UTE subtraction method can highlight the CEP region.
3D UTE[50]	Assess CEP abnormality in the lumbar spine in vivo.	3 T Philips (Achieva); TR/TE = 4.8/0.14 msec; Resolution = 0.6 × 0.6 × 2.4 mm^3; scan time = 18 minutes 47 seconds.	Advantages: • High SNR for CEP region. Limitations: • Limited CNR between CEP and BMF.	• 3D UTE can detect CEP abnormality. • CEP abnormality is BMI and age-related. • CEP abnormality is associated with IVD degeneration.
3D FS-UTE[48]	Investigate associations between CEP thickness and IVD degeneration.	3 T GE (Discovery MR 750 W); TR/TE = 12/0.075 msec; resolution = 0.5 × 0.5 × 1.5 mm^3.	Advantages: • High CNR between CEP and BMF. Limitations: • Fat suppression efficiency may be limited due to the weakness of the FS technique.	• Mean CEP thickness was 0.74 mm. • CEP is thicker at the periphery and thinner in the central portion. • Heterogeneity in CEP thickness may be an indicator of IVD degeneration.
3D UTE dual-echo subtraction[47]	Improve the contrast between the CEP and adjacent tissues.	3 T (GE Discovery 750 W); TR = 12.5 msec; TE = 0.03/6 msec; in-plane resolution = 1 × 1 mm^2; scan time = 2 minutes 48 seconds.	Advantages: • Increased CEP-NP contrast. Limitations: • Limited CEP-BMF contrast. • Suffer susceptibility-induced signal variations.	Subtracted UTEimages provide good contrast for the assessment of CEP damage and IVD degeneration.

TABLE 1. Continued

Techniques	Applications	Scanner and Key Sequence Parameters	Advantages and Limitations	Main Findings
3D IR-FS-UTE[52]	High-contrast CEP imaging.	3 T (GE MR750); TR/TI = 1200/600 msec; TE = 0.032 msec; in-plane resolution = 0.75 × 0.75 mm^2 (ex vivo)/0.875 × 0.875 mm^2 (in vivo); Scan time: 1 hour 22 minutes (ex vivo)/9 minutes 52 seconds (in vivo)	Advantages: • Highlight CEP signals with simultaneous signal suppression of the NP and BMF. Limitations: • Long scan time. • Fat suppression is limited.	• The IR-FS-UTE sequence was able to provide high-contrast CEP imaging. • Various CEP damages had been detected.
3D DIR-UTE[51]	High-contrast CEP imaging.	3 T (GE MR750); $TR/TI_1/TI_2$ = 1500/610/150 msec; TE = 0.032 msec; in-plane resolution = 0.375 × 0.375 mm^2 (Ex vivo)/0.875 × 0.875 mm^2 (in vivo); scan time = 16 minutes (ex vivo)/10 minutes (in vivo)	Advantages: • Highlight CEP signals with simultaneous signal suppression of the NP and BMF. Limitations: • Long scan time.	• DIR-UTE image showed the highest CNRs of CEP-BMF and CEP-NP. • DIR-UTE technique detected various CEP abnormalities.

SPGR = spoiled gradient echo; TE = echo time; TR = repetition time; CEP = cartilaginous endplate; NP = nucleus pulposus; BMF = bone marrow fat; IVD = intervertebral disc; FS = fat suppression; NEX = number of excitation; SNR = signal to noise ratio; UTE = ultrashort echo time; FS-LS-UTE = fat suppression long T_2 suppression ultrashort echo time; BMI = body mass index; CNR = contrast to noise ratio; IR = inversion recovery; DIR = dual adiabatic inversion recovery.

[a]The long T_2 tissue suppression (LS) was achieved by a rectangular 90° pulse before the half RF excitation pulses to selectively excite tissues or fluids with a long T_2 after which the signal from these components was dephased by use of a gradient.

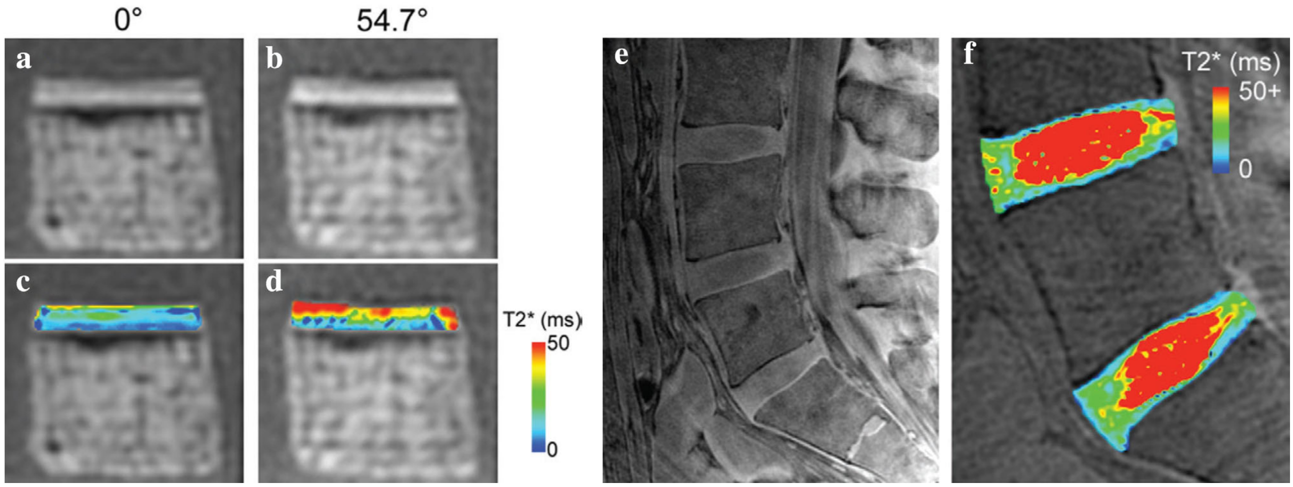

FIGURE 7: Ultrashort echo time (UTE) T_2* mapping of two different spine samples. UTE images (a, b) and T_2* maps (c, d) of a cartilaginous endplate (CEP) sample imaged at 0° and 54.7° relative to the main magnetic field. Greater signal intensity and higher T_2* value are shown at 54.7°. UTE image and T_2* mapping of another lumbar spine specimen (L3-S1) of a 37-year-old male donor are shown in (e) and (f) respectively. The inferior CEP of L5-S1 intervertebral disc shows greater signal intensity (e) and T_2* value (f) due to its angle being approximately the magic angle. Reproduced with permission from Fields et al.[38]

sufficiently short TE. When combined with the FS module, the contrast between CEP and BMF is significantly improved in FS-SPGR. Due to its short scan time and clinical availability, SPGR-based techniques are promising tools for morphological CEP imaging alongside conventional T_1w- and T_2w-FSE imaging. The UTE-based sequences (eg, Dual-echo UTE, T_1w-FS-UTE, IR-FS-UTE, and DIR-UTE) generate higher contrast to noise ratios between CEP and adjacent tissues compared to the SPGR sequences due to their much shorter TEs. However, their limited clinical availability currently hinders their widespread clinical use.

Quantitative MRI of the Cartilaginous Endplate

As mentioned above, both SPGR and UTE sequences have been successfully used for morphological CEP imaging. Moreover, there is a growing interest in quantitative MRI of the CEP due to its sensitivity to biochemical changes in CEP tissues. SPGR- and UTE-based quantitative MRI techniques for mapping T_2*/T_2, T_1, $T_{1\rho}$, perfusion properties, magnetization transfer ratio (MTR) and diffusion properties of the CEP are described below.

T_2 AND T_2 MEASUREMENTS.* T_2* mapping offers insights into the integrity of collagen and the mobility of water.[37,61] Changes in T_2* reflect alterations in water content and the extent to which water is "bound" or "free." T_2* values are calculated by fitting the signal decay equation: $S(\mathrm{TE}) = S_0 e^{(-\mathrm{TE}/T_2^*)}$ with signal on MR images acquired with multi echoes, where S_0 is the equilibrium magnetization, and $S(\mathrm{TE})$ is the measured MR signal. T_2 measurement uses a similar strategy.

The multi-echo UTE method is commonly used for CEP T_2* mapping. In 2014, Bae et al reported a mean CEP T_2* value of 2.9 msec, measured with 2D multi-echo UTE sequences.[43] In 2015, Fields et al measured the T_2* values of CEP tissue with 2D multi-echo FUTE sequences.[38] Their results revealed that the CEP T_2* values were orientation dependent: CEP T_2* values measured at 54.7° (i.e., magic angle) relative to the main magnetic field direction were greater than those measured at 0° (~21.8 msec vs. 10 msec) (Fig. 7c,d). Furthermore, CEP T_2* values measured at the magic angle exhibited significant correlations with glycosaminoglycan content, collagen-to-glycosaminoglycan ratio, and water content, whereas these correlations were not significant at 0° or 90°. For in vivo scanning, the orientations of the L4-L5 and L5-S1 CEPs are closest to the magic angle (Fig. 7e,f). Consequently, T_2* values of the L4-L5 and L5-S1 CEPs are likely to be longer than those of CEPs in other spinal segments that have the same degeneration grade. The longer values of T_2* correlate with CEP biochemical composition.

In 2020, Wang et al utilized the 3D UTE Cones method to measure the spatial distribution of T_2* values within the CEP and correlated this with IVD degeneration in different age groups.[42] Their findings revealed that CEP T_2* values were highest centrally and lowest posteriorly (ranging from 14.2 msec to 23.9 msec), suggesting regional variations in the CEP's biochemical composition. Additionally, in the youngest group with mild-to-moderate degenerated IVDs (Pfirrmann grade II-III), low CEP T_2* values were associated with more severe IVD degeneration, although this association was not observed in older groups. In 2022, Bonnheim et al conducted CEP T_2* mapping with the 3D UTE Cones sequence in 60 patients with chronic low back pain.[40] CEP T_2* values ranged from 2 msec to 33 msec were associated with NP $T_{1\rho}$ values, indicating that CEP compositional changes reflect the severity of IVD degeneration. In 2023, Bonnheim et al proposed a deep learning-based automatically CEP segmentation and CEP T_2* calculation model.[54] This model eliminated measurement deviations introduced by the analysts' subjectivity during the manually segmentation, enabling efficient, objective, and accurate computation of CEP T_2* values. They tried to group the CEPs regarding T_2* values using predicted segmentations generated by the proposed model, and the group predictions achieved diagnostic sensitivities of 0.77–0.86.

T_2 mapping reflects water content, proteoglycan fiber networks, and molecular interactions.[61] T_2 values can serve as a biomarker for assessing IVD degeneration.[33] In 2020, Cao et al performed CEP T_2 calculations in 130 patients using a multi-echo SE pulse sequence (i.e., Carr-Purcell-Meiboom-Gill [CPMG] sequence).[39] However, the estimated T_2 values, ranging from 42.47 msec to 66.34 msec, appeared to be overestimated. The in-plane resolution of their images was 1.2×1.6 mm^2, which was considerably greater than the mean thickness of the CEP (0.62 mm).[3] In addition, the region of interest was located at the center of the CEP (the thinnest region of the CEP). Therefore, the signal within the region of interest was inevitably contaminated by the adjacent long T_2 tissues, such as the NP and bone BMF. Moreover, the CPMG sequence in a clinical scanner with relatively long TEs may not capture sufficient CEP signals, and the resulting low signal to noise ratio (SNR) images may lead to inaccurate T_2 quantification. In 2022, Athertya et al utilized a 3D CPMG sequence to measure T_2 relaxation times of a human thoracic spine sample.[41] The in-plane resolution of the sequence was 0.15×0.15 mm^2, which was sufficiently high for accurate CEP T_2 mapping. Their measured mean CEP T_2 value of 17.79 msec was much lower than Cao et al's.

With the most reported CEP T_2* values no less than 4 msec,[38,40,42] both SPGR and UTE pulse sequences with echo times less than 4 msec are feasible for CEP morphology imaging. However, UTE is preferable for the T_2* mapping as it can provide more fitting data with shorter TEs improving T_2* fitting accuracy. On the other hand, SPGR sequences are more time efficient than UTE sequences, making them more suitable for clinical application.

T_1 MEASUREMENT. T_1 mapping has found utility in assessing cartilage degeneration,[62] with correlations of T_1 with water content.[63] Nevertheless, application of T_1 mapping to IVD degeneration assessment, in particular the CEP, remains relatively unexplored.

In 2013, Moon et al conducted a study in which they scanned a healthy cadaveric lumbar disc sample using a 2D inversion recovery spin echo (IR-SE) sequence with 10 different inversion times at both 7 T and 3 T magnetic field strengths. Their results showed mean CEP T_1 values at 7 T of 775 msec (Fig. 8e) and at 3 T of 540 msec.[17] However, the use of a long TR to ensure full recovery of the longitudinal magnetization resulted in a long total scan time, rendering the method impractical for in vivo applications.

In 2021, Lombardi et al utilized a 3D UTE actual flip angle and variable flip angle (UTE-AFI-VFA) method[64] to measure the CEP T_1 values for spine samples at 3 T (Fig. 8a–d).[52] Their findings revealed a mean CEP T_1 value of 360 msec, which was notably shorter than the 540 msec reported by Moon et al.[17] This may be attributed to the relatively long TE (i.e., 13 msec) used with the 2D IR-SE sequence. This sequence can only capture signals from free water within the CEP and is unable to detect signals from bound water components which typically have much shorter T_1 values compared to free water. Consequently, the T_1 values obtained through IR-SE may appear relatively prolonged. The UTE-AFI-VFA technique concurrently assessed T_1 values for both bound and free water components and thus includes shorter T_1 components.

$T_{1\rho}$ MEASUREMENT. $T_{1\rho}$ presents the spin–lattice relaxation in the rotating frame in the presence of an external spin-lock RF pulse, reflecting low-frequency motional biological processes, including those arising from macromolecule-water interactions.[65] $T_{1\rho}$ provides sensitive detection of proteoglycan loss at early stages of cartilage degeneration.[66]

In 2020, Ling et al measured CEP $T_{1\rho}$ values using a 2D FSE sequence in both rhesus monkeys and humans and revealed a notable decrease in $T_{1\rho}$ values in the older group compared to the younger group.[67] In 2021, Wei et al employed a 3D adiabatic $T_{1\rho}$ prepared UTE (UTE-Adiab-$T_{1\rho}$) pulse sequence (Fig. 9a) to measure CEP $T_{1\rho}$ values in IVDs with different degrees of degeneration (Fig. 9b–e).[55] This UTE-Adiab-$T_{1\rho}$ pulse sequence employed trains of adiabatic full passage (AFP) pulses for spin locking and UTE data acquisition. The study showed significant correlations between both superior and inferior CEP $T_{1\rho}$ values and the severity of IVD degeneration, suggesting that CEP $T_{1\rho}$ values could serve as biomarkers of IVD degeneration. In addition, Adiab-$T_{1\rho}$ measurements are less sensitive to the magic angle effect than T_2* measurements, potentially making them more reliable biomarkers for CEP assessment.[68]

Given the short T_2* of CEP tissue, combining spin-locking preparation with a short TE acquisition scheme is essential for measuring CEP $T_{1\rho}$. Similar to cartilage, the CEP contains both short- and long-T_2 water components. Multi-compartment $T_{1\rho}$ quantification conducted with either a continuous wave-prepared UTE sequence or a UTE-Adiab-$T_{1\rho}$ sequence has the potential to demonstrate this.[69]

MAGNETIZATION TRANSFER IMAGING. MTR is correlated with collagen concentration and tissue matrix integrity.[70] Given the collagen-rich nature of the CEP, measuring

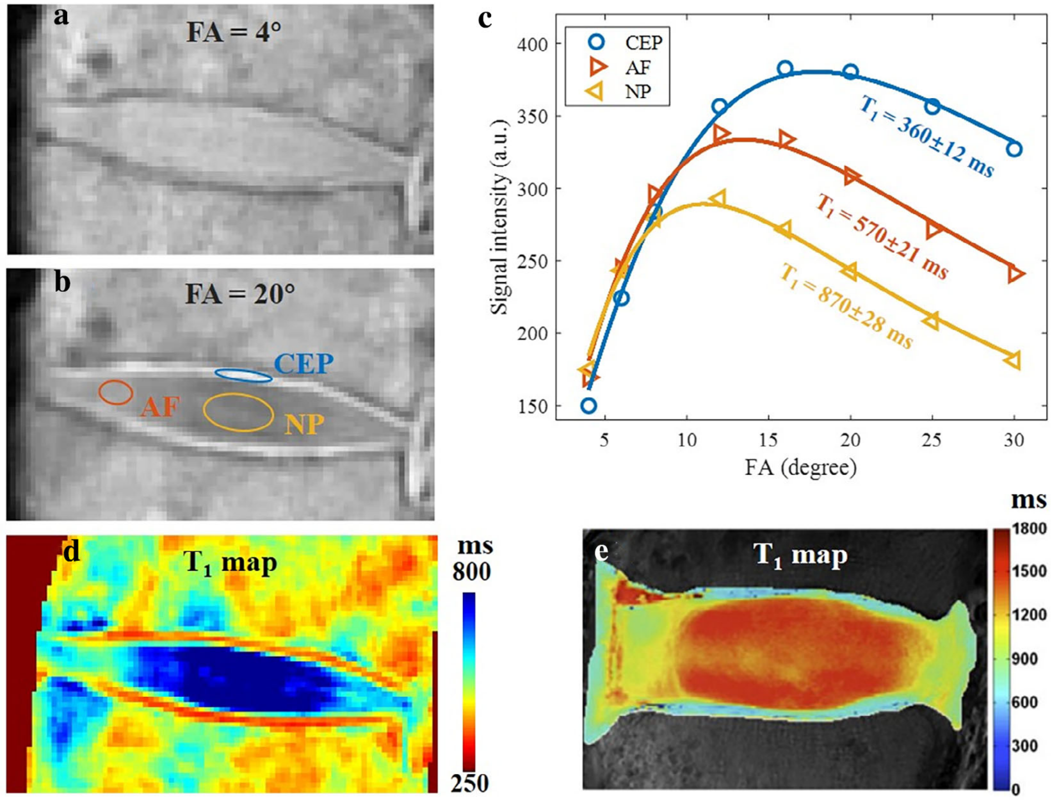

FIGURE 8: T_1 mapping of intervertebral disc (IVD) samples. Panels (a) and (b) are representative ultrashort echo time variable flip angle (UTE-VFA) images with flip angles (FAs) of 4° and 20°, respectively, at 3 T. Panel (c) shows the corresponding fitting curves and mean T_1 values of the cartilaginous endplate (CEP), nucleus pulposus (NP), and annulus fibrosus (AF), and (d) is the T_1 map of this IVD sample measured with the UTE-VFA method with B_1 correction. (e) shows the T_1 map of a normal IVD sample measured at 7 T. (a–d) reproduced with permission from Lombardi et al.[52] (e) reproduced with permission from Moon et al.[17]

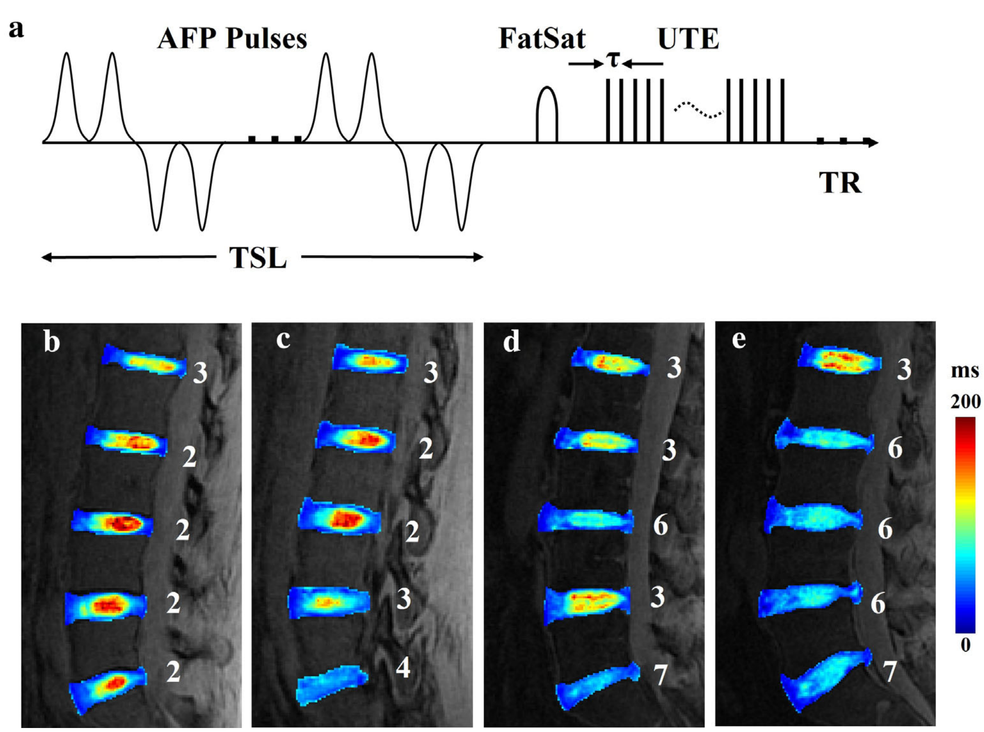

FIGURE 9: In vivo lumbar intervertebral disc (IVD) $T_{1\rho}$ maps acquired with a 3D adiabatic $T_{1\rho}$ prepared ultrashort echo time (UTE-Adiab-$T_{1\rho}$) sequence. Panel (a) is the pulse sequence diagram for the UTE-Adiab-$T_{1\rho}$ sequence. $T_{1\rho}$ contrast is generated by a train of adiabatic full passage (AFP) pulses during the spin-locking time (TSL). This is followed by a fat saturation (FatSat) pulse and multiple UTE acquisitions. Representative $T_{1\rho}$ maps of lumbar IVDs with different modified Pfirrmann grades from four volunteers are shown from (b) to (e). The modified Pfirrmann grades are labeled next to the corresponding IVD. Reproduced with permission from Wei et al.[55]

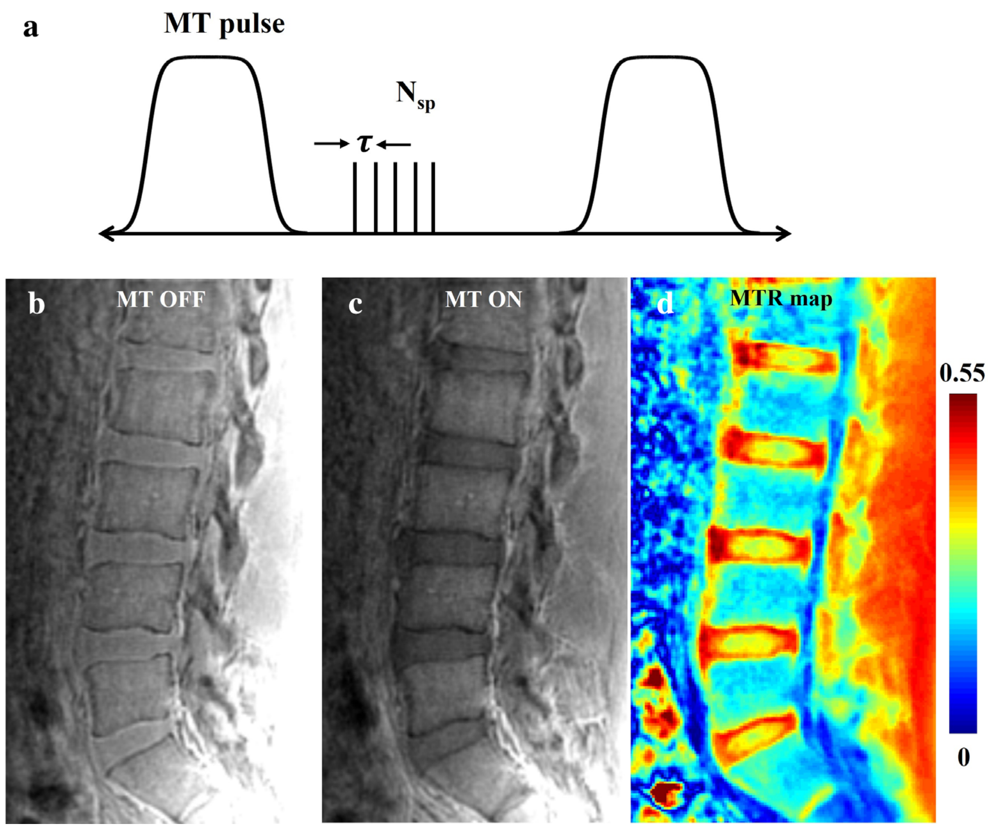

FIGURE 10: In vivo lumbar spine imaging with a magnetization transfer (MT) prepared ultrashort echo time (MT-UTE) sequence. Panel (a) is the pulse sequence diagram for the MT-UTE sequence. Lumbar spine images of a 25-year-old male volunteer obtained with MT off and on are shown in (b) and (c), respectively. The corresponding MT ratio (MTR) map is shown in (d). This MTR map reveals higher MTR values in the cartilaginous endplate and annulus fibrosus compared to the nucleus pulposus, indicating greater collagen content in the cartilaginous endplate and annulus fibrosus.

CEP MTR may serve as a biomarker of degenerative changes in IVD involving collagen.

Figure 10 shows a representative lumbar CEP MTR map from a healthy 25-year-old male volunteer using an MT-prepared UTE (MT-UTE) sequence. The color MTR map of the lumbar IVDs reveals higher MTR values in the CEP and AF compared to the NP, indicating greater collagen content in the CEP and AF. This finding is consistent with previous biochemical studies,[6,71] confirming the value of CEP MTR mapping with the MT-UTE method.

PERFUSION MEASUREMENT. Perfusion and fluid transport within the CEP are crucial for nutrition supply and metabolic transportation. Studying the perfusion of the CEP can help reveal the relationship between CEP permeability and IVD degeneration. Muftuler et al applied a dynamic contrast-enhanced (DCE) MRI protocol to study perfusion and fluid transport mechanisms in the endplates of IVDs.[72] They observed a low enhancement peak and no noticeable washout in the CEP DCE MRI signal, with DCE enhancement in the CEP increased with Pfirrmann grade. In 2019, Arpinar et al examined DCE-MRI enhancement with 3D SPGR pulse sequence in endplate regions of IVDs.[44] Their findings revealed significant associations between Oswestry Disability Index (ODI) scores and enhancement in the CEP regions within the most degenerated IVDs.

These studies suggest that DCE-MRI enhancement in the CEP region is associated with IVD degeneration and low back pain (as measured by the ODI). However, it is important to note that these studies were conducted ex vivo, and there is currently no widely accepted technique for assessing endplate perfusion in vivo.

DIFFUSION TENSOR IMAGING. Diffusion tensor imaging (DTI) reveals random movement of water molecules within tissues utilizing diffusion-sensitive gradient pairs. This allows evaluation of water diffusion characteristics and directional anisotropy.[73,74] Quantitative scalar metrics derived from the DTI model, such as the fractional anisotropy (FA), mean diffusivity (MD), axial diffusivity (AD), and radial diffusivity (RD), are known to correlate with tissue microstructure.[74] Understanding the microstructure of the IVD is crucial for regenerative medicine and the development of tissue engineering-based treatments for IVD disease.[75] Recently, DTI tractography has been employed to delineate various tissues within the knee joint, including the articular cartilage,

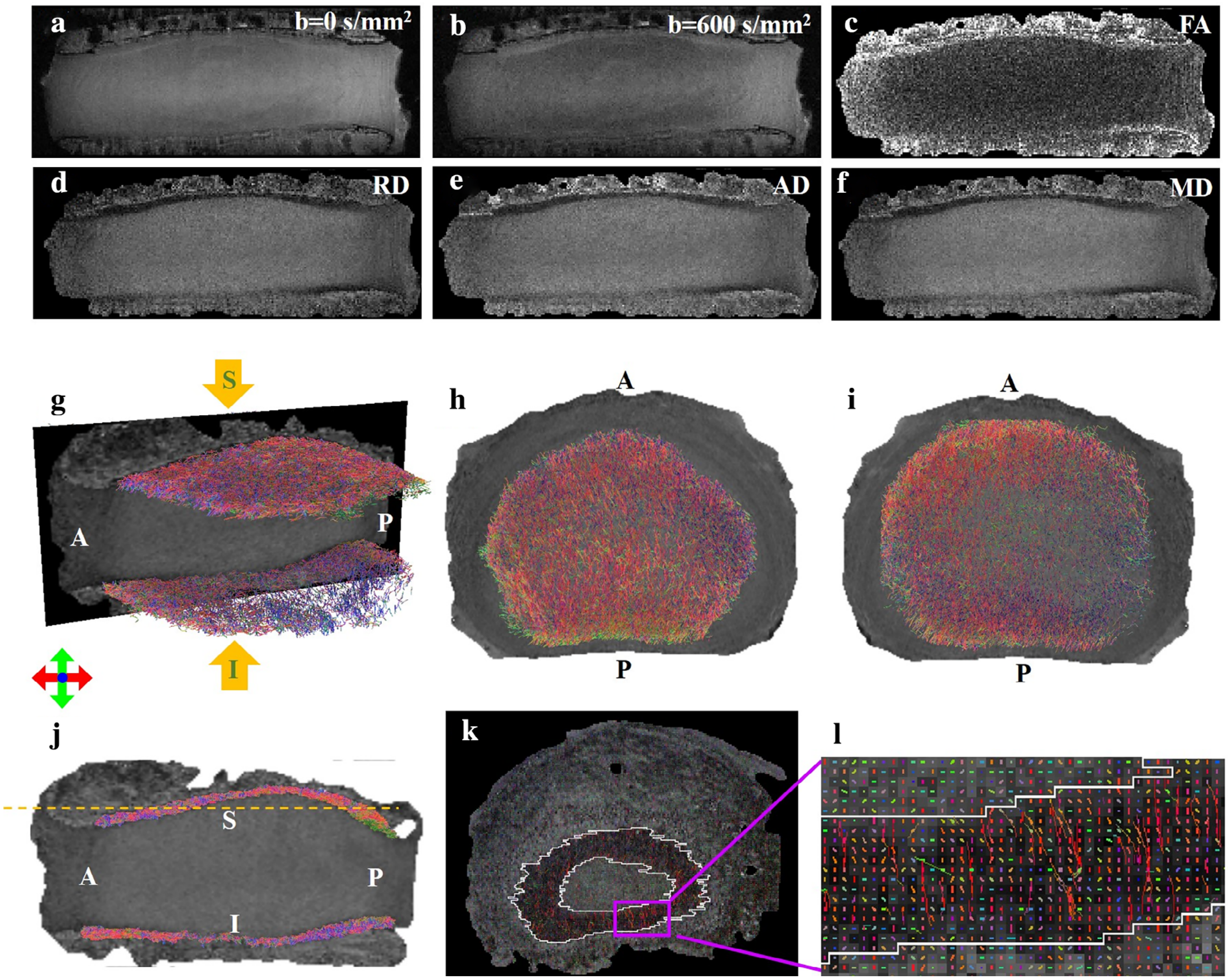

FIGURE 11: Diffusion tensor imaging (DTI) of an intervertebral disc sample. Representative diffusion-weighted spin echo images are shown in the coronal plane with $b = 0\ s/mm^2$ (a) and $b = 600\ s/mm^2$ (b), along with the corresponding DTI parameter maps for fractional anisotropy (FA) (c), radial diffusivity (RD) (d), axial diffusivity (AD) (e), and mean diffusivity (MD) (f). CEP fibers are presented in a 3D view (g), across axial (h, i) and sagittal (j) planes. The panel (k) provides a fiber orientation map of the superior cartilaginous endplate. An enlarged view of the fiber orientation map is shown in the pink box (l). Dominant alignment of fibers in the anterior–posterior direction is observed. Red for anterior–posterior orientation; green for right–left orientation; blue for superior–inferior orientation. A = anterior; P = posterior; S = superior; I = interior. Reproduced with the permission from Wei et al.[80]

anterior/posterior cruciate ligament, growth plate, and meniscus, and IVD's AF.[76–79]

Most recently, Wei et al pioneered the utilization of a 3D Stejskal-Tanner diffusion-weighted spin-echo pulse sequence with high resolution and DTI model to derive quantitative scalar DTI metrics (Fig. 11c–f) and to track the fiber orientation and structure (Fig. 11g–l) of in a human CEP sample.[80] Their results revealed that the CEP contrasts on the RD, AD, and MD maps were more pronounced compared to diffusion-weighted images and FA maps. Additionally, their findings showed a consistent conclusion with histological studies that the predominant orientation of CEP fibers is parallel and horizontal in the anterior–posterior direction. Compared with histological methods, the advantages of DTI tractography is noninvasive and can visualize the intact CEP fiber architecture.

Table 2 summarizes quantitative CEP imaging techniques. CEP T_2^* values, measured with multi-echo UTE, ranged from 2.9 msec to 43 msec.[38,43] The CEP fiber direction variation relative to the B_0 direction, resulted in a wide range of T_2^* values due to the magic angle effect. Multi-echo SE and CPMG sequences were employed to measure CEP T_2 values in vivo and ex vivo, respectively.[39,41] However, in vivo CEP T_2 values are likely overestimated,[39] and more accurate ex vivo measurements were time-consuming with very high image resolution. In vivo CEP T_2 mapping remains challenging, and a T_2-prepared UTE sequence may be a promising technique for accurate CEP T_2 measurement in future studies. Currently, all CEP T_1 measurement studies have been performed on ex vivo samples, with no in vivo CEP T_1 values reported so far. The UTE-AFI-VFA method is more promising than the IR-SE technique for in vivo CEP T_1

TABLE 2. Quantitative MRI Techniques for Cartilaginous Endplate Imaging

Techniques	Applications	Scanner and Key Sequence Parameters	Advantages and Limitations	Main Findings
Multi-echo UTE sequences[38,40,42,43,54]	Quantify the CEP T_2* value.	Reference 38: 3 T GE (Discovery MR750w); TR = 30 msec; TE = 0.075, 2, 5, 12, 18 msec; resolution = 0.22 × 0.22 × 0.8 mm^3/0.22 × 0.22 × 0.9 mm^3; FS every fourth spoke. Reference 42: 3 T GE (Discovery MR 750); TR = 32 msec; TE = 0.244, 5.2, 10.2, 15.2, 20.2, 25.2 msec; (in vivo); TE = 0.308, 2.7, 5.0, 7.4, 14.4, 16.8, 19.1, 21.5, 23.8, 26.2 (ex vivo); resolution = 0.5 × 0.5 × 3 mm^3; Reference 43: Scanner type and sequence parameters were not given. Reference 40: 3 T GE (Discovery MR 750); TR = 32 msec; TE = 0.244, 5.2, 10.2, 15.2, 20.2, 25.2 msec; resolution = 0.5 × 0.5 × 1 mm^3; Reference 54: 3 T GE (Discovery MR 750); TR = 32 msec; TE = 0.244, 5.2, 10.2, 15.2, 20.2, 25.2 msec; in-plane resolution = 1 × 1 mm^2.	Advantages: • UTE provides more data with shorter TE, improving T_2* fitting accuracy. Limitations: • Due to the magic angle effect, CEP T_2* measurement is relevant to IVD levels. • Long scan time.	• Mean CEP T_2* was subject to the magic angle effect: higher at 54.7° (21.8 msec) than at 0° and 90° (~10 msec). T_2* ranged from 4 to 43 msec at 54.7° and 4 to 16 msec at 0° and 90°.[38] • CEP T_2* value was highest centrally and lowest posteriorly.[42] • CEP T_2* values ranged from 14.2 to 23.9 msec.[42] • Lower CEP T_2* values associated with more severe IVD degeneration.[42] • Mean CEP T_2* values ranged from 2 to 33 msec, and were associated with NP $T_{1\rho}$ values.[40] • Mean CEP T_2* value could be derived from the deep learning model.[39,54]
CPMG sequences[39,41]	Quantify the CEP T_2 value.	Reference 39: 3 T GE (MR 750 W); TR = 1000 msec; TE = 8.5, 16.9, 25.4, 33.9, 42.3, 50.8, 67.7 msec; in-plane resolution = 1.17 × 1.56 mm^2; scan time = 6 minutes 26 seconds.	Advantages: • Acceptable scan time for in vivo scanning.[39] • Sufficiently high resolution for CEP imaging.[41]	• T_2 values of CEP within different degeneration levels ranged from 42.47 to 66.34 msec.[39] • Significant differences of CEP T_2 values in different IVD degeneration levels.[39]

TABLE 2. Continued

Techniques	Applications	Scanner and Key Sequence Parameters	Advantages and Limitations	Main Findings
		Reference 41: 3 T (Bruker BioSpec); TR = 1000 msec; TE = 2.8, 8.4, 14, 19.6, 25.2, 30.8, 42, 47.6, 53.2 msec; resolution = 0.15 × 0.15 × 0.5 mm^3; scan time = 28 hours 32 minutes.	Limitations: • Low resolution, and relatively long TEs (low SNR).[39] • Long scan time.[41]	• CEP T_2 values of L4-L5, and L5-S1 segments were highly correlated with IVD degeneration levels.[39] • Demonstrate the feasibility of ex vivo CEP T_2 measurement with the CPMG sequence.[41] • Mean CEP T_2 value was 17.79 msec.[41]
IR-SE sequences[48]	Quantify the CEP T_1 value.	7 T (Simens, Magnetom); 3 T (Siemens, Tim Trio); TR = 5100 msec; TI: 10 TIs between 33 and 5000 msec; TE = 11/13 msec (7 T/3 T); in-plane resolution = 0.2 × 0.2 mm^2.	Advantages: • Available on clinical scanners. Limitations: • Long scan time is not suitable for in vivo scanning. • TEs were relatively long for CEP signal detection.	Mean CEP T_1 value was 775 msec at 7 T and 540 msec at 3 T.
UTE-AFI-VFA sequences[52]	Quantify the CEP T_1 value.	3 T (GE MR750); AFI: TR1/TR2 = 20/100 msec; FA = 45°; VFA: TR/TE = 20/0.032 msec; FA = 4°, 6°, 8°, 12°, 16°, 20°, 25°, 30°; resolution = 0.4 × 0.4 × 2 mm^3; scan time = 1 hour 10 minutes	Advantages: • Short TE suitable for CEP signal detection. Limitations: • Relatively long scan time.	Mean CEP T_1 value was 360 msec at 3 T.
2D $T_{1\rho}$ weighted FSE sequences[67]	Quantify the CEP $T_{1\rho}$ value.	1.5 T (Philips); TR/TE = 800/8 msec; in-plane resolution = 0.59 × 1.17 mm^2; TSL = 11, 22, 32, 43, 54, 65, 76, 85 msec.	Advantages: • Detect compositional change in CEP. Limitations: • Relatively long TE for CEP signal detection.	• CEP $T_{1\rho}$ values showed a correlation with IVD degeneration levels. • Mean CEP $T_{1\rho}$ value ranged from 28.94 to 35.82 msec.

TABLE 2. Continued

Techniques	Applications	Scanner and Key Sequence Parameters	Advantages and Limitations	Main Findings
3D UTE-Adiab-$T_{1\rho}$ sequences[55]	Quantify the CEP $T_{1\rho}$ value.	3 T (GE, MR750); TR/TE = 2000/0.1 msec; TSL = 0, 34.56, 69.12, 103.68 msec; in-plane resolution = 0.875 × 0.875 mm^2; scan time = 17 minutes 36 seconds.	Advantages: • Using an Adiabatic spin-locking pulse train makes the sequence less sensitive to the magic angle effect. • Detect compositional change in CEP. • Short TE achieved high SNR of the CEP region. Limitations: • Relatively long scan time.	• Mean CEP $T_{1\rho}$ value ranged from 35.6 to 43.5 msec. • CEP $T_{1\rho}$ is sensitive to IVD degeneration.
MT-UTE sequence	Quantify the CEP MTR value.	3 T (GE, MR750); FA = 700° (MT on)/400° (MT off); frequency offset = 2 kHz; TR/TE = 100/0.032 msec; in-plane resolution: 0.875 × 0.875 mm^2; slice thickness = 3 mm, scan time 47 seconds	Advantages: • Detect macromolecular content changes. • Short TE for CEP imaging. Limitations: • Not applicable since no studies have been performed for the clinical validation.	• MT-UTE was able to map the CEP MTR. • CEP MTR is higher than that of NP due to the higher collagen content.
GRE-based DCE MRI[44,72]	Quantify the dynamic contrast enhancement to evaluate the solute transport mechanism in the CEP.	Reference 72: 3 T (Philips, Achieva); TR/TE = 3.4/1.2 msec; 22 dynamic frames with 36.4 seconds frame rate; scan time: 13 minutes 35 seconds with 15 seconds pause for injection.	Advantages: • Provide functional information on CEP. Limitations:	• There was a positive association between CEP DCE-MRI enhancement and IVD degeneration level.[72]

TABLE 2. Continued

Techniques	Applications	Scanner and Key Sequence Parameters	Advantages and Limitations	Main Findings
		Reference 44: 3 T (GE, MR Discovery 750); 3D SPGR TR = 4 msec; TE_1/TE_2 = 1.1/2.2 msec; in-plane resolution = 1 × 1 mm^2; 25 dynamic frames with a 28 seconds frame rate; 8 seconds delay for contrast agent injection.	• Need to inject contrast agent.	• DCE-MRI enhancement in the CEP region was associated with greater disability scores.[44]
Diffusion-weighted SE sequence[80]	Measure the diffusion tensor parameters and construct the fiber structure to evaluate CEP diffusivity and microstructure.	3 T (Bruker, BioSpec); TR/TE = 500/9 msec; b = 0 and 600 s/mm^2 (in 15 directions); resolution = 0.2 × 0.2 × 0.2 mm^3; scan time = 135 hours.	Advantages: • Provide diffusion properties and fiber directions Limitations: • Long scan time.	• The RD, AD and MD maps of the CEP were obtained; • The CEP fiber structure was consistent with previous histological findings.

UTE = ultrashort echo time; TE = echo time; TR = repetition time; FS = fat suppression; CEP = cartilaginous endplate; IVD = intervertebral disc; SE = spin echo; CPMG = Carr-Purcell-Meiboom-Gill; AFI = actual flip angle imaging; VFA = variable flip angle; FA = flip angle; TSL = spin locking time; SNR = signal to noise ratio; MT = magnetization transformation; MTR = magnetization transformation ratio; GRE = gradient echo; DCE = dynamic contrast enhancement; RD = radial diffusivity; AD = axial diffusivity; MD = mean diffusivity.

measurement due to its time efficiency and accuracy (shorter TE).[17,52] For CEP $T_{1\rho}$ measurement, the UTE-Adiab-$T_{1\rho}$ sequence is superior to the continuous wave-based $T_{1\rho}$ weighted FSE sequence, as it is less sensitive to the magic angle effect and offers the advantage of a short TE.[55,68] SPGR-based DCE MRI of the CEP is promising and may provide valuable functional information about endplates.[72] The future development of UTE-based DCE MRI may provide more reliable information about CEP function. The MT-UTE for CEP MTR mapping and SE-based DTI for CEP fiber structure imaging are still in the pilot study phase and require further technical and clinical validation.[80]

Discussion and Conclusion

This review summarizes the currently available MRI techniques for CEP imaging. Due to the thinness and short T_2* of the CEP, effective imaging sequences need to have high image resolution and short TEs. High-resolution SPGR and UTE are the most commonly used sequences for morphological and quantitative CEP MR imaging.

Morphological CEP imaging techniques hold promise in clinical practice. Endplate irregularities have been recognized to be associated with back pain and injury.[13,26,81] According to Berg-Johannsen et al's classification of endplate irregularities, conditions such as tidemark avulsion, CEP-bone avulsion, and traumatic injury may involve CEP damages.[27] However, CEP signals are not detectable on clinical T_1w- and T_2w-FSE images, making it difficult to classify endplate irregularities, especially in vivo. Fortunately, recently developed high-contrast CEP imaging techniques, including T_1w-FS-UTE,[51] IR-FS-UTE,[52] DIR-UTE,[51] and FS-SPGR,[17,45] are feasible for detecting various endplate and disc irregularities. These abnormalities include CEP discontinuities,[45,52] CEP disruptions,[45] disc vacuum,[45] CEP fracture,[51] CEP disappearance,[51,52] and endplate fracture.[52] Most recently, Wáng recommended high-resolution UTE CEP imaging techniques for classifying two primary Schmorl's node types.[82] These studies demonstrate that morphological CEP imaging techniques provide additional information on the disc-vertebral junction beyond what is available from clinical spine imaging sequences and hold great promise for clinical practice.

Although there are only a few quantitative CEP imaging studies, the most frequently studied compositional biomarker, T_2*, has been proven to be associated with biochemical changes in IVD[38,40] and degeneration severity.[42] Moreover, recent advances in deep learning techniques have achieved good performance in CEP segmentation, T_2* quantification, and patient grouping.[54] Additionally, CEP $T_{1\rho}$ values have shown significant correlations with IVD degeneration, age, and low back pain symptoms.[55] These findings suggest that quantitative CEP imaging techniques may provide promising biomarkers for clinical diagnosis and treatment monitoring of back pain. Further research utilizing other quantitative MRI parameters, such as T_1, MT, perfusion, and diffusion, is warranted to understand compositional changes in CEP pathology, particularly in vivo.[41,80]

Most CEP imaging studies were conducted on 3 T, with a few on 1.5 T or 7 T. Theoretically, all these CEP imaging techniques can be performed adequately on 1.5 T. Compared to 3 T, sequence parameters at 1.5 T will need to be adjusted to account for differences in MR properties, such as T_1 and T_2. The relatively low image SNR at lower field MRI may not be an issue due to recent advances in denoising techniques using deep learning.[83] These techniques should be applicable to different spine sections, including the cervical, thoracic, and lumbar spine. Some sequence parameter adjustments, such as field of view and resolution, may be needed due to the size differences of the IVDs within different spine sections.

Artificial intelligence and machine learning are expected to be of considerable value in MRI of the CEP.[84,85] Additionally, sequences with TEs of 0.1 msec or less, such as single point imaging (SPI),[86] water- and fat-suppressed proton projection MRI (WASPI),[87] sweep imaging with Fourier transformation (SWIFT),[88] and zero echo time (ZTE),[89] may also have the potential to provide both morphological evaluation and quantitative measurements of the CEP tissue, similar to UTE sequences.

In summary, morphological imaging techniques have shown great promise for clinical translation and could be valuable additions to current clinical protocols. Quantitative CEP MRI is still in its early stages, and further studies are warranted.

Acknowledgments

The authors acknowledge grant support from the National Institutes of Health (F32AG082458 and R01AR079484) and GE Healthcare, and the ChatGPT from the OpenAI team for providing valuable assistance throughout the process of writing this paper.

References

1. Deyo RA, Mirza SK, Martin BI. Back pain prevalence and visit rates estimates from U.S. National Surveys, 2002. Spine 2006;31:2724-2727.
2. Martin BI, Richard Deyo MA, Sohail Mirza MK, et al. Expenditures and health status among adults with Back and neck problems. JAMA 2008; 299:656-664.
3. Roberts S, Menage J, Urban JPG. Biochemical and structural properties of the cartilage end-plate and its relation to the intervertebral disc. Spine 1989;14:166-174.
4. Luoma K, Riihimäki H, Luukkonen R, Raininko R, Viikari-Juntura E, Lamminen A. Low back pain in relation to lumbar disc degeneration. Spine 2000;25:487-492.
5. Zheng CJ, Chen J. Disc degeneration implies low back pain. Theor Biol Med Model 2015;12:24.

6. Raj PP. Intervertebral disc: Anatomy-physiology-pathophysiology-treatment. Pain Pract 2008;8:18-44.

7. Roberts S, Urban JPG, Evans H, Eisenstein SM. Transport properties of the human cartilage endplate in relation to its composition and calcification. Spine 1996;21:415-420.

8. Crump KB, Bermudez-lekerika P, Mcsweeney T, et al. Cartilaginous endplates: A comprehensive review on a neglected structure in intervertebral disc research. JOR Spine 2023;6:e1294.

9. González Martínez E, García-Cosamalón J, Cosamalón-Gan I, Blanco ME, García-Suarez O, Vega JA. Biology and mechanobiology of the intervertebral disc. Neurocirugia 2017;28:135-140.

10. Urban JPG, Smith S, Fairbank JCT. Nutrition of the intervertebral disc. Spine 2004;29:2700-2709.

11. Wong J, Sampson SL, Bell-Briones H, et al. Nutrient supply and nucleus pulposus cell function: Effects of the transport properties of the cartilage endplate and potential implications for intradiscal biologic therapy. Osteoarthr Cartil 2019;27:956-964.

12. Setton LA, Zhu W, Weidenbaum M, Ratcliffe A, Mow VC. Compressive properties of the cartilaginous end-plate of the baboon lumbar spine. J Orthop Res 1993;11:228-239.

13. Lama P, Zehra U, Balkovec C, Harding IJ, Dolan P, Adams MA. Significance of cartilage endplate within herniated disc tissue. Eur Spine J 2014;23:1869-1877.

14. Farshad-Amacker NA, Hughes A, Herzog RJ, Seifert B, Farshad M. The intervertebral disc, the endplates and the vertebral bone marrow as a unit in the process of degeneration. Eur Radiol 2017;27:2507-2520.

15. Delucca JF, Peloquin JM, Smith LJ, Wright AC, Vresilovic EJ, Elliott DM. MRI quantification of human spine cartilage endplate geometry: Comparison with age, degeneration, level, and disc geometry. J Orthop Res 2016;34:1410-1417.

16. Beattie EE, Yoder JH, Moon SM, Vresilovic EJ, Elliott DM, Wright AC. Quantification of intervertebral disc cartilaginous endplate morphology using MRI. *38th annual northeast bioengineering conference. USA*: IEEE; 2012. p 103-104.

17. Moon SM, Yoder JH, Wright AC, Smith LJ, Vresilovic EJ, Elliott DM. Evaluation of intervertebral disc cartilaginous endplate structure using magnetic resonance imaging. Eur Spine J 2013;22:1820-1828.

18. Wu Y, Cisewski SE, Wegner N, et al. Region and strain-dependent diffusivities of glucose and lactate in healthy human cartilage endplate. J Biomech 2016;49:2756-2762.

19. Huang CY, Gu WY. Effects of mechanical compression on metabolism and distribution of oxygen and lactate in intervertebral disc. J Biomech 2008;41:1184-1196.

20. Bernick S, Cailliet R. Vertebral end-plate changes with aging of human vertebrae. Spine 1982;7:97-102.

21. Bernick S, Cailliet R, Levy V. The maturation and aging of the vertebrae of marmosets. Spine 1980;5:519-524.

22. Aigner T, Greskötter KR, Fairbank JCT, Von Der Mark K, Urban JPG. Variation with age in the pattern of type X collagen expression in normal and scoliotic human intervertebral discs. Calcif Tissue Int 1998;63:263-268.

23. Wade KR, Robertson PA, Broom ND. On how nucleus-endplate integration is achieved at the fibrillar level in the ovine lumbar disc. J Anat 2012;221:39-46.

24. Wade KR, Robertson PA, Broom ND. A fresh look at the nucleus-endplate region: New evidence for significant structural integration. Eur Spine J 2011;20:1225-1232.

25. Delucca JF, Cortes DH, Jacobs NT, Vresilovic EJ, Duncan RL, Elliott DM. Human cartilage endplate permeability varies with degeneration and intervertebral disc site. J Biomech 2016;49:550-557.

26. Fields AJ, Liebenberg EC, Lotz JC. Innervation of pathologies in the lumbar vertebral end plate and intervertebral disc. Spine J 2014;14:513-521.

27. Berg-Johansen B, Jain D, Liebenberg EC, et al. Tidemark avulsions are a predominant form of endplate irregularity. Spine 2018;43:1095-1101.

28. Pfirrmann CWA, Metzdorf A, Zanetti M, Hodler J, Boos N. Magnetic resonance classification of lumbar intervertebral disc degeneration. Spine 2001;26:1873-1878.

29. Amin RM, Andrade NS, Neuman BJ. Lumbar disc herniation. Curr Rev Musculoskelet Med 2017;10(4):507-516.

30. Yang B, Wendland MF, O'Connell GD. Direct quantification of intervertebral disc water content using MRI. J Magn Reson Imaging 2020;52:1152-1162.

31. Krug R, Joseph GB, Han M, et al. Associations between vertebral body fat fraction and intervertebral disc biochemical composition as assessed by quantitative MRI. J Magn Reson Imaging 2019;50:1219-1226.

32. Chiu EJ, Newitt DC, Segal MR, Hu SS, Lotz JC, Majumdar S. Magnetic resonance imaging measurement of relaxation and water diffusion in the human lumbar intervertebral disc under compression in vitro. Spine 2001;26:437-444.

33. Marinelli NL, Haughton VM, Muñoz A, Anderson PA. T2 relaxation times of intervertebral disc tissue correlated with water content and proteoglycan content. Spine 2009;34:520-524.

34. Borthakur A, Maurer PM, Fenty M, et al. T1ρ magnetic resonance imaging and discography pressure as novel biomarkers for disc degeneration and low back pain. Spine 2011;36:2190-2196.

35. Blumenkrantz G, Zuo J, Li X, Kornak J, Link TM, Majumdar S. In vivo 3.0-tesla magnetic resonance T1ρ and T2 relaxation mapping in subjects with intervertebral disc degeneration and clinical symptoms. Magn Reson Med 2010;63:1193-1200.

36. Bouhsina N, Decante C, Hardel JB, et al. Comparison of MRI T1, T2, and T2* mapping with histology for assessment of intervertebral disc degeneration in an ovine model. Sci Rep 2022;12:1-12.

37. Welsch GH, Trattnig S, Paternostro-Sluga T, et al. Parametric T2 and T2* mapping techniques to visualize intervertebral disc degeneration in patients with low back pain: Initial results on the clinical use of 3.0 Tesla MRI. Skeletal Radiol 2011;40:543-551.

38. Fields AJ, Krug R, Lotz JC. Cartilaginous end plates: Quantitative MR imaging with very short Echo times—Orientation dependence and correlation with biochemical composition. Radiology 2015;274:482-489.

39. Cao Y, Guo Q, Wan Y. Significant association between the T2 values of vertebral cartilage endplates and Pfirrmann grading. Orthop Surg 2020;12:1164-1172.

40. Bonnheim NB, Wang L, Lazar AA, et al. The contributions of cartilage endplate composition and vertebral bone marrow fat to intervertebral disc degeneration in patients with chronic low back pain. Eur Spine J 2022;31:1866-1872.

41. Athertya JS, Lombardi AF, Wong J, et al. Quantitative MR imaging of whole intervertebral disc: A pre-clinical sample study. *Proceedings of the 31st Annual Meeting of ISMRM*. London: Curran Associates Inc; 2022. p 2330.

42. Wang L, Han M, Wong J, et al. Evaluation of human cartilage endplate composition using MRI: Spatial variation, association with adjacent disc degeneration, and in vivo repeatability. J Orthop Res 2020;39:1470-1478.

43. Bae WC, Biswas R, Chen K, Chang EY, Chung CB. UTE MRI of the Osteochondral junction. Curr Radiol Rep 2014;2:35.

44. Arpinar VE, Muftuler LT, Gliedt JA, King JA. Oswestry Disability Index scores correlate with MRI measurements in degenerating intervertebral discs and endplates. Eur J Pain 2020;24:346-353.

45. Athertya JS, Statum S, Chen X, et al. Evaluation of spine disorders using high contrast imaging of the cartilaginous endplate (CEP). Front Physiol 2024;15:15.

46. Kakitsubata Y, Theodorou DJ, Theodorou SJ, et al. Cartilaginous endplates of the spine: MRI with anatomic correlation in cadavers. J Comput Assist Tomogr 2002;26:933-940.

47. Ji Z, Li Y, Dou W, Zhu Y, Shi Y, Zou Y. Ultra-short echo time MR imaging in assessing cartilage endplate damage and relationship between

its lesion and disc degeneration for chronic low back pain patients. BMC Med Imaging 2023;23:1-8.

48. Berg-Johansen B, Han M, Fields AJ, et al. Cartilage endplate thickness variation measured by ultrashort Echo-time MRI is associated with adjacent disc degeneration. Spine 2018;43:E592-E600.
49. Bae WC, Statum S, Zhang Z, et al. Morphology of the cartilaginous endplates in human intervertebral disks with ultrashort echo time MR imaging. Radiology 2013;266:564-574.
50. Law T, Anthony M, Chan Q, et al. Ultrashort time-to-echo MRI of the cartilaginous endplate: Technique and association with intervertebral disc degeneration. J Med Imaging Radiat Oncol 2013;57:427-434.
51. Athertya JS, Lo J, Chen X, et al. High contrast cartilaginous endplate imaging in spine using three dimensional dual-inversion recovery prepared ultrashort echo time (3D DIR-UTE) sequence. Skeletal Radiol 2024;53:881-890.
52. Lombardi AF, Wei Z, Wong J, et al. High contrast cartilaginous endplate imaging using a 3D adiabatic inversion-recovery-prepared fat-saturated ultrashort echo time (3D IR-FS-UTE) sequence. NMR Biomed 2021;34(10):e4579.
53. Gatehouse PD, He T, Hughes SPF, Bydder GM. MR imaging of degenerative disc disease in the lumbar spine with ultrashort TE pulse sequences. Magn Reson Mater Phys Biol Med 2004;16:160-166.
54. Bonnheim NB, Wang L, Lazar AA, et al. Deep-learning-based biomarker of spinal cartilage endplate health using ultra-short echo time magnetic resonance imaging. Quant Imaging Med Surg 2023;13:2807-2821.
55. Wei Z, Lombardi AF, Lee RR, et al. Comprehensive assessment of in vivo lumbar spine intervertebral discs using a 3D adiabatic T1ρ prepared ultrashort echo time (UTE-Adiab-T1ρ) pulse sequence. Quant Imaging Med Surg 2021;12:269-280.
56. Haase A, Frahm J, Matthaei D, Hanicke W, Merboldt KD. FLASH imaging rapid NMR imaging using low flip-angle pulses. J Magn Reson 1986;67:258-266.
57. Ma Y, Jang H, Jerban S, et al. Making the invisible visible — Ultrashort echo time magnetic resonance imaging: Technical developments and applications. Appl Phys Rev 2022;9:041303.
58. Gurney PT, Hargreaves BA, Nishimura DG. Design and analysis of a practical 3D cones trajectory. Magn Reson Med 2006;55:575-582.
59. Du J, Hamilton G, Takahashi A, Bydder M, Chung CB. Ultrashort echo time spectroscopic imaging (UTESI) of cortical bone. Magn Reson Med 2007;58:1001-1009.
60. Du J, Bydder M, Takahashi AM, Carl M, Chung CB, Bydder GM. Short T2 contrast with three-dimensional ultrashort echo time imaging. Magn Reson Imaging 2011;29:470-482.
61. Krinner S, Trattnig S. T2 and T2* mapping. Curr Radiol Rep 2014;2:1-9.
62. Nebelung S, Sondern B, Oehrl S, et al. Functional MR imaging mapping of human articular cartilage response to loading. Radiology 2017; 282:464-474.
63. Shiquetomi-Medina JM, Gottliebsen M, Kristiansen MS, et al. Water-content calculation in growth plate and cartilage using MR T1-mapping design and validation of a new method in a porcine model. Skeletal Radiol 2013;42:1413-1419.
64. Ma YJ, Zhao W, Wan L, et al. Whole knee joint T1 values measured in vivo at 3T by combined 3D ultrashort echo time cones actual flip angle and variable flip angle methods. Magn Reson Med 2019;81:1634-1644.
65. Wáng Y-XJ, Zhang Q, Li X, Chen W, Ahuja A, Yuan J. T1ρ magnetic resonance: Basic physics principles and applications in knee and intervertebral disc imaging. Quant Imaging Med Surg 2015;5:858-885.
66. Regatte RR, Akella SVS, Wheaton AJ, et al. 3D-T1ρ-relaxation mapping of articular cartilage: In vivo assessment of early degenerative changes in symptomatic osteoarthritic subjects. Acad Radiol 2004;11:741-749.
67. Ling Z, Li L, Chen Y, et al. Changes of the end plate cartilage are associated with intervertebral disc degeneration: A quantitative magnetic resonance imaging study in rhesus monkeys and humans. J Orthop Translat 2020;24:23-31.
68. Wu M, Ma Y, Kasibhatla A, et al. Convincing evidence for magic angle less-sensitive quantitative T1ρ imaging of articular cartilage using the 3D ultrashort echo time cones adiabatic T1ρ (3D UTE cones-Adiab T1ρ) sequence. Magn Reson Med 2020;84:2551-2560.
69. Sharafi A, Xia D, Chang G, Regatte RR. Biexponential T1ρ relaxation mapping of human knee cartilage in vivo at 3T. NMR Biomed 2017;30:1-11.
70. Wang C, Witschey W, Goldberg A, Elliott M, Borthakur A, Reddy R. Magnetization transfer ratio mapping of intervertebral disc degeneration. Magn Reson Med 2010;64:1520-1528.
71. Eyre DR, Muir H. Quantitative analysis of type I and type II collagens in human intervertebral at various ages. Biochim et Biophys Aeta 1977; 492:29-42.
72. Muftuler LT, Jarman JP, Yu HJ, Gardner VO, Maiman DJ, Arpinar VE. Association between intervertebral disc degeneration and endplate perfusion studied by DCE-MRI. Eur Spine J 2015;24:679-685.
73. Mukherjee P, Chung SW, Berman JI, Hess CP, Henry RG. Diffusion tensor MR imaging and fiber tractography: Technical considerations. Am J Neuroradiol 2008;29:843-852.
74. Mukherjee P, Berman JI, Chung SW, Hess CP, Henry RG. Diffusion tensor MR imaging and fiber tractography: Theoretic underpinnings. Am J Neuroradiol 2008;29:632-641.
75. Kandel R, Roberts S, Urban JPG. Tissue engineering and the intervertebral disc: The challenges. Eur Spine J 2008;17(SUPPL. 4):480-491.
76. Wang N, Mirando AJ, Cofer G, Qi Y, Hilton MJ, Johnson GA. Diffusion tractography of the rat knee at microscopic resolution. Magn Reson Med 2019;81:3775-3786.
77. Shen J, Zhao Q, Qi Y, Cofer G, Johnson GA, Wang N. Tractography of porcine meniscus microstructure using high-resolution diffusion magnetic resonance imaging. Front Endocrinol 2022;13(May):1-9.
78. Wang N, Mirando AJ, Cofer G, Qi Y, Hilton MJ, Johnson GA. Characterization complex collagen fiber architecture in knee joint using high-resolution diffusion imaging. Magn Reson Med 2020;84:908-919.
79. Stein D, Assaf Y, Dar G, et al. 3D virtual reconstruction and quantitative assessment of the human intervertebral disc's annulus fibrosus: A DTI tractography study. Sci Rep 2021;11:1-11.
80. Wei Z, Yang W, Moazamian D, et al. Tractography of human intervertebral disc using high resolution diffusion tensor imaging. *Proceedings of the 33rd Annual Meeting of ISMRM*. Singapore: Curran Associates Inc; 2024. p 4160.
81. Thompson KJ, Dagher AP, Eckel TS, Clark M, Reinig JW. Modic changes on MR images as studied with provocative diskography: Clinical relevance – A retrospective study of 2457 disks. Radiology 2009; 250:849-855.
82. Wáng YXJ. Cartilaginous endplate coverage of developmental Schmorl's node and the relevance of this in Schmorl's node etiology-based classification. Quant Imaging Med Surg 2024;14:4288-4303.
83. Manjón JV, Coupe P. MRI denoising using deep learning. *Lecture notes in computer science. Volume 11075 LNCS. Spain*: Springer Verlag; 2018. p 12-19.
84. Galbusera F, Casaroli G, Bassani T. Artificial intelligence and machine learning in spine research. JOR Spine 2019;2(1):e1044.
85. Cui Y, Zhu J, Duan Z, Liao Z, Wang S, Liu W. Artificial intelligence in spinal imaging: Current status and future directions. Int J Environ Res Public Health 2022;19(18):11708.
86. Fang Z, Hoepfel D, Winter K. Application of single point imaging (SPI) to solid state materials. Magn Reson Imaging 2001;19:501-503.
87. Cao H, Ackerman JL, Hrovat MI, Graham L, Glimcher MJ, Wu Y. Quantitative bone matrix density measurement by water- and fat-suppressed proton projection MRI (WASPI) with polymer calibration phantoms. Magn Reson Med 2008;60:1433-1443.
88. Idiyatullin D, Corum C, Park JY, Garwood M. Fast and quiet MRI using a swept radiofrequency. J Magn Reson 2006;181:342-349.
89. Weiger M, Pruessmann KP, Hennel F. MRI with zero echo time: Hard versus sweep pulse excitation. Magn Reson Med 2011;66:379-389.